Observation of orbital order in the Van der Waals material $1T$-$TiSe_2$

Yingying Peng,[1,*] Xuefei Guo,[2] Qian Xiao,[1] Qizhi Li,[1] Jörg Strempfer,[3] Yongseong Choi,[3] Dong Yan,[4,5] Huixia Luo,[4] Yuqing Huang,[1] Shuang Jia,[1] Oleg Janson,[6] Peter Abbamonte,[2] Jeroen van den Brink,[6,7,8] and Jasper van Wezel[8,†]

[1] *International Center for Quantum Materials, School of Physics, Peking University, Beijing 100871, China*
[2] *Department of Physics and Materials Research Laboratory, University of Illinois, Urbana, IL 61801, USA*
[3] *Advanced Photon Source, Argonne National Laboratory, Argonne, Illinois 60439, USA*
[4] *School of Materials Science and Engineering, State Key Laboratory of Optoelectronic Materials and Technologies, Sun Yat-Sen University, Guangzhou 510275, China*
[5] *Key Laboratory of Functional Molecular Solids, Ministry of Education, College of Chemistry and Materials Science, Anhui Normal University, Wuhu 241002, China*
[6] *Institute for Theoretical Solid State Physics, IFW Dresden, Helmholtzstr. 20, 01069 Dresden, Germany*
[7] *Würzburg-Dresden Cluster of Excellence ct.qmat, TU Dresden, 01069 Dresden, Germany*
[8] *Institute for Theoretical Physics Amsterdam, University of Amsterdam, Science Park904, 1098 XH Amsterdam, The Netherlands*

(Dated: February 11, 2022)

Besides magnetic and charge order, regular arrangements of orbital occupation constitute a fundamental order parameter of condensed matter physics. Even though orbital order is difficult to identify directly in experiments, its presence was firmly established in a number of strongly correlated, three-dimensional Mott insulators. Here, reporting resonant X-ray scattering experiments on the layered Van der Waals compound $1T$-$TiSe_2$, we establish the emergence of orbital order in a weakly correlated, quasi-two-dimensional material. Our experimental scattering results are consistent with first-principles calculations that bring to the fore a generic mechanism of close interplay between charge redistribution, lattice displacements, and orbital order. It demonstrates the essential role that orbital degrees of freedom play in $TiSe_2$, and their importance throughout the family of correlated Van der Waals materials.

Keywords: orbital order, charge density wave, Van der Waals materials

INTRODUCTION

Quasi two-dimensional Van der Waals (VdW) materials are layered solids with strong in-plane covalent bonding and weak interlayer VdW interactions, that have become a focal area for materials research in recent years [1–10]. The success of graphene – which stems from the paradigmatic VdW material graphite – in particular, triggered a search for similar VdW materials that can be exfoliated to the monolayer limit, but which harbour physical properties beyond those of graphene [11, 12]. Magnetic ordering for example, has been observed in the VdW materials CrX_3 (X = Cl, Br, I) [2–4], $Cr_2Ge_2Te_6$ [5] and $NiPS_3$ [6].

The family of transition-metal dichalcogenides (TMDC) is a particularly promising group of VdW materials, that can be straightforwardly prepared in atomically thin configurations and device settings [12]. They typically harbour multiple competing and coexisting phases of matter, which allow a fine tuning of the phase diagram and material properties in response to external stimuli like pressure, intercalation, or gating [13–15]. At the same time, however, uncertainty and controversy surround the ground state order in several TMDC. This is especially striking in the case of $1T$-$TiSe_2$, whose charge order (CDW) below $T_{\mathrm{CDW}} \simeq 200\,\mathrm{K}$ was discovered decades ago [16]. Debates about its nature and driving mechanism, however, are only recently converging towards a combination of exciton formation and lattice effects stabilising a condensate of particle-hole pairs [17–25], while debate about its potential chirality continues until the present day [26–31]. Within this context, we establish here that additionally, the electronic ground state in $1T$-$TiSe_2$ has a non-trivial orbital structure.

At the centre of the rich phase diagram and versatility of TMDC materials, but also of their controversies, lie the transition-metal d-orbitals. Their spatially compact but not fully localised electronic wave functions allow small changes in the occupation of these orbitals to have a strong effect on the atomic displacement of neighbouring chalcogens, on the distribution of electron charges between atoms, on the coupling of electronic excitations to phonons, and even on the structuring of spins [26, 32–35]. Unveiling any patterns of orbital occupation therefore offers a novel crucial element for understanding the nature and emergence of order in transition-metal dichalcogenides.

That the orbital degree of freedom of electrons in a solid material can be ordered in the same fashion as the electron's charge or spin, was pointed out in the 1970s [36, 37]. Even if electrons in solids form bands and delocalize from the nuclei, in Mott insulators they retain their three fundamental quantum numbers: spin, charge and orbital. This observation sparked a field of research that has gone on to produce a number of important results regarding the cooperative and often concomitant ordering of these degrees of freedom: just as spins can

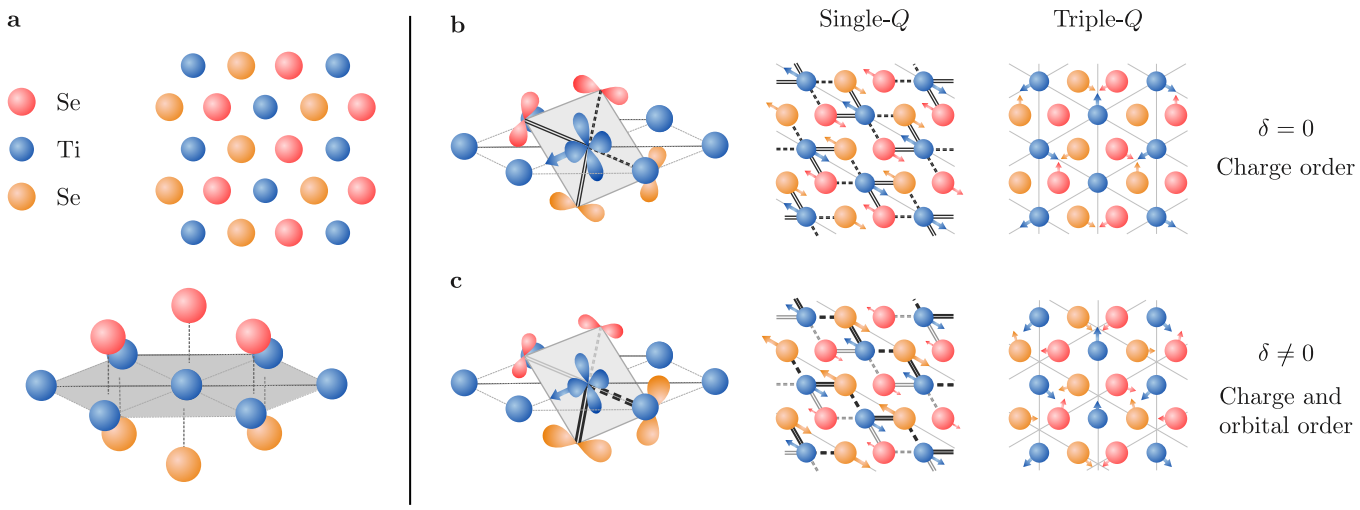

FIG. 1. **Charge and orbital order in $1T$-$TiSe_2$.** (a) Top-view and three-dimensional sketch of the atomic structure within a single layer of $1T$-$TiSe_2$ in the high-temperature phase (space group 164, $P\bar{3}m1$). (b) The charge ordered phase without relative phase shifts (space group 165, $P\bar{3}c1$). The local charge transfer process for one of the CDW components and all orbitals involved in it are shown in the three-dimensional structure, followed by a top view of the displacements and charge transfers in a single CDW component, and finally the full displacement pattern in the triple-Q structure actually realised in $TiSe_2$. Extrema of the CDW are indicated by faint grey lines and atomic displacements by arrows (exaggerated for clarity). Double lines indicate an electronic bonding state between neighbouring atoms, while dashed lines depict an electronic anti-bonding state. (c) The orbital ordered state resulting from relative phase shifts δ between CDW components (space group 5, $C2$). The sliding of a single component causes the charge transfer processes to be centered on either the upper or lower Se layer. As a result, the atomic displacements and orbital occupations associated with different CDW components differ in amplitude. This results in a slight alteration to the distortion pattern, as well as an ordered redistribution of electronic charge among the titanium t_{2g} orbitals.

spontaneously organise into regular arrangements and produce myriad types of magnetism, orbital degrees of freedom can also spontaneously order into regular patterns. Such orbital order has been identified using polarised neutron diffraction to measure its effect on the magnetic form factor in for example K_2CuF_4 [38], or by measuring how it influences charge distributions in x-ray or electron diffraction in materials like $NdSr_2Mn_2O_7$ [39]. The first direct observation of orbital order, however, was established for $LaMnO_3$ and $La_{0.5}Sr_{1.5}MnO_4$ using resonant X-ray scattering (RXS) experiments [40, 41]. All of these materials are three-dimensional Mott insulators, characterised by strong Coulomb interactions and correspondingly large variations of orbital occupancy.

Here, we use resonant X-ray scattering measurements at the titanium K-edge to reveal the onset of long-range orbital order among the titanium d-orbitals of the weakly-coupled Van der Waals material $1T$-$TiSe_2$, within its well-known charge ordered phase. The orbitals that order in $TiSe_2$ mediate a strong interaction with spin, charge and lattice degrees of freedom. The orbital order thus not only represents a new ordered phase of matter for VdW materials, but also offers an inroad for engineering complex phase diagrams and devices with beyond-graphene capability.

ORBITAL ORDER IN $TiSe_2$

The quasi-two-dimensional layers of $1T$-$TiSe_2$ consist of titanium atoms in a triangular arrangement, sandwiched between similar planes of selenium atoms and separated from neighbouring sandwich layers by a large Van der Waals gap, as shown schematically in Fig. 1a [42]. The octahedral coordination of selenium atoms around each titanium splits the titanium d-shell into three t_{2g} and two e_g orbitals. The subsequent hybridization between low-energy t_{2g} orbitals and selenium p-orbitals lies at the root of charge and orbital order in $TiSe_2$ [26].

Cooling down from high temperatures, the uniform, metallic state gives way to a well-known charge ordered (CDW) state at $T_{\mathrm{CDW}} \simeq 200\,\mathrm{K}$, with atomic displacements (shown in Fig. 1b) known from neutron diffraction experiments [16]. Owing to the lattice symmetry, the charge order in $TiSe_2$ consists of three simultaneous one-dimensional, or single-Q, charge density waves, related to one another by 120° rotations. In each of these, symmetry dictates that electronic charge is transferred within a specific set of titanium t_{2g} and selenium p-orbitals, as indicated in Fig. 1b [26]. The atomic displacements in each of the single-Q CDW components can then be understood as the shortening (extension) of Ti-Se bonds

with electronic (anti)bonding states. Notice that as long as the three-fold rotational symmetry of the lattice remains unbroken, all t_{2g} orbitals remain equally occupied.

The three components of the charge ordered state are not independent, and influence one another through local Coulomb interactions. On the basis of theoretical considerations it has been proposed that these yield a second phase transition in $TiSe_2$, in which the three CDW components slide by different amounts in order to minimize the real-space overlap of electronic charge [26, 27]. This results in a redistribution of charge between different t_{2g} orbitals, and thus an orbital ordered (OO) state that breaks both the three-fold rotational and inversion symmetries of the high-temperature phases. The atomic displacements associated with the shifting CDW components reflect the broken symmetries, and yield a low-temperature configuration shown in Fig. 1c. However, the changes in atomic displacement upon entering the OO phase may be expected to be exceedingly small, and evade detection in scanning-tunneling microscopy (STM) and x-ray diffraction experiments [16, 29].

The actual presence of broken inversion symmetry associated with orbital order in $TiSe_2$ has been the subject of intense debate [29–31]. On the one hand, there is indirect evidence of a phase transition at temperatures slightly below T_{CDW} [27], and STM experiments reporting the formation of domains that appear to have different senses of handedness [43]. These are contested however by other groups who observe no evidence of broken inversion symmetry in STM or other probes [29]. The paradox is further fuelled by lack of any direct impact of the breakdown of inversion on scattering experiments, and the practical complication of bulk probes necessarily averaging over many domains of different handedness, thus precluding any direct measurement of broken inversion symmetry. Recently, photogalvanic effect measurements were able to conclusively show inversion symmetry to be broken in the low-temperature phase of samples cooled through their ordering transition in the presence of a strong circularly polarized light field [44]. Because of the active training, however, these results do not rule out the possibility that untrained samples of $TiSe_2$ remain inversion symmetric.

Here, we find that orbital order, rather than the breakdown of inversion symmetry, is actually the main characteristic of the low-temperature phase of $TiSe_2$. The mechanism of CDW components sliding by different amounts under the influence of Coulomb interactions and hence giving rise to spatial modulations in the occupation of orbitals, is generic for multi-component CDW materials, and has been suggested to be at play in the same form in other TMDC compounds, such as 2H-TaS_2, as well as some elemental materials, like Se, Te, and Po [26, 34, 45, 46]. The RXS experiments presented here, supported by first-principles calculations, show direct experimental evidence for the presence of an orbital ordered phase in $TiSe_2$. Crucially, because the observed signal is insensitive to the handedness of any domains, it is not necessary to train the sample with an applied field, allowing us to detect symmetry breaking that is truly spontaneous.

X-RAY SCATTERING

Orbital order in 3d transition-metal compounds can be probed by RXS at the main K-edge corresponding to the $1s \rightarrow 4p$ transition [47, 48]. The contribution of Ti 3d orbitals to the pre-edge of this transition stems primarily from their hybridization with ligand Se 4p orbitals that are in turn hybridized with 4p orbitals of neighboring Ti atoms. In addition, lack of inversion symmetry allows for some direct hybridization between Ti 3d and 4p orbitals at the same site. Hence, we performed RXS measurements at the Ti K-edge to investigate the ordering of Ti 3d orbitals of t_{2g} symmetry (see Methods section for sample preparation and experimental set-up). In agreement with RXS measurements at the Se K-edge [49], the observed CDW reflections may be divided into qualitatively different groups, based on their energy dependence. Unlike the Se-based measurements, however, we find that the different energy profiles of the Ti K-edge reflections allow us to assign them to distinct scattering processes and yield direct evidence for the presence of orbital order.

The first group of reflections contains conventional CDW peaks, like the $(0.5, 0.5, 0.5)$ reflection shown in Fig. 2a, which are also visible in non-resonant scattering experiments. Their energy line shape is similar to that of the primary Bragg peaks, included for comparison in Fig. 2c. These signals are dominated by Thomson scattering from atomic cores, and give a direct measure of the lattice displacements in the CDW phase. Since all electrons on the Ti atoms participate in this type of scattering process, it yields a large overall intensity. It does not have a strong energy dependence, except for a sharp suppression near the resonant edge, where incoming x-rays can be resonantly absorbed. Fig. 2e shows the integrated intensity of the peak in panel a. Fitting with a universal power-law function (see Methods section for details) yields an estimated transition temperature of $T_{\mathrm{CDW}} \sim 193\,\mathrm{K}$, which is consistent with resistivity measurements on a sample from the same batch.

Intriguingly, we identified a second group of RXS signals at points in k-space where reflections are absent in non-resonant experiments, like $(0.5, 0, 0.5)$ shown in Fig. 2b (another example, $(2.5, 0, 0.5)$, is shown in the Supplemental Material). The structure factor at these momenta is strictly zero as long as the crystal structure of $TiSe_2$ is either $P\bar{3}m1$ or $P\bar{3}c1$, corresponding to the symmetries of the high-temperature phase and the CDW state without orbital order respectively (see Supplemental Material for details of the calculation). The origin

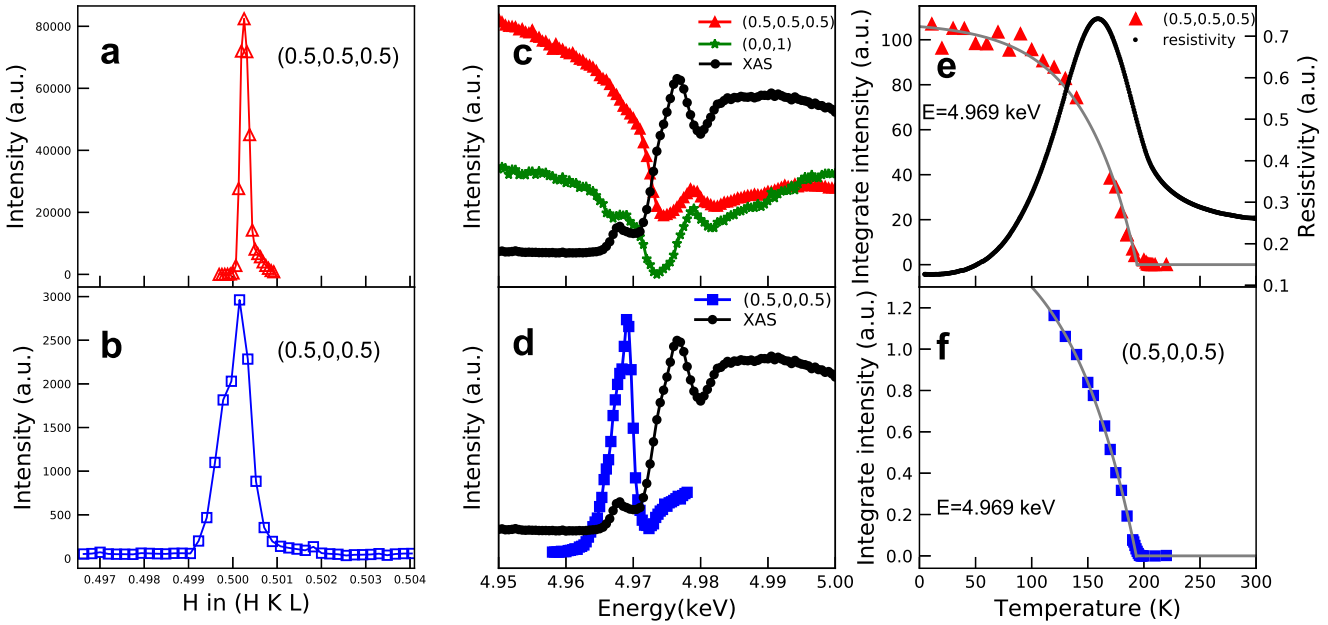

FIG. 2. **Charge density wave and orbital order in $TiSe_2$ and their energy- and temperature-dependence measured by RXS at the Ti K-edge.** (a, b) H cuts at 11 K for $(0.5, 0.5, 0.5)$ and $(0.5, 0, 0.5)$, respectively. (c, d) Corresponding energy scans near Ti K-edge. The X-ray Absorption Spectrum (XAS) at the Ti K-edge is shown for comparison, as is the energy scan for the $(0, 0, 1)$ Bragg peak. (e, f) Temperature dependence at 4.969 keV of the peaks at $(0.5, 0.5, 0.5)$ and $(0.5, 0, 0.5)$ respectively. The resistivity measurement is displayed in (e) for comparison. The gray solid lines are fits to the data showing a transition temperature T_{cdw} ∼193 K.

for the reflections in the present experiment can be clarified from their energy dependence. Unlike what would be expected from Thomson scattering, these signals have a strong, resonant peak at the pre-edge of the Ti K-edge, as shown in Fig. 2d. This is typical for reflections originating in transitions between specific orbital states, involving only a few electrons that can be efficiently excited only near resonance [50]. For this type of reflection, the local density of states dominates the energy dependence of the scattering intensity.

The presence of a second group of reflections, originating from transitions between specific orbital states, implies that Titanium atoms with the same number of electrons, whose structure factors cancel in Thomson scattering, must have inequivalent orbital structures that allow these reflections under resonant conditions. In other words, the orbital occupations of the Titanium atoms follows a regular pattern with lower symmetry than the high-temperature state and conventional CDW phase. The observation of peaks like $(0.5, 0, 0.5)$ and $(2.5, 0, 0.5)$, with energy dependencies dominated by orbital-specific transitions, thus constitutes direct evidence of orbital order in the low-temperature phase of $TiSe_2$. Based on fits of the thermal evolutions of integrated intensities for these new reflections, shown in Fig. 2f, we find the onset temperature of the novel orbital ordered state and the conventional CDW phase to be indistinguishable within the experimental resolution.

Although the orbital order is primarily manifested in the occupation of titanium t_{2g} orbitals, it also has an effect on atomic displacements. This is evidenced in yet a third class of reflections that we observe, whose energy dependence indicates a combination of Thomson and orbital-specific scattering (for example, the peak $(0.5, 0.5, 2.5)$ is shown in the Supplemental Material). These reflections are significantly enhanced compared to non-resonant experiments near the Ti K-edge, but also show the largely energy-independent background characteristic of atomic scattering. The enhancement of these reflections can be viewed as a secondary effect of the onset of orbital order, and showcase the strong coupling between orbital, lattice, and charge degrees of freedom.

FIRST-PRINCIPLES RESULTS

A Ginzburg-Landau theory analysis of $TiSe_2$ predicts orbital order to emerge when different CDW components obtain phase shifts relative to one another [26]. Adding corresponding phase shifts to the atomic displacements, gives a model for the atomic configuration of the OO phase (see Supplemental Material for details). To obtain

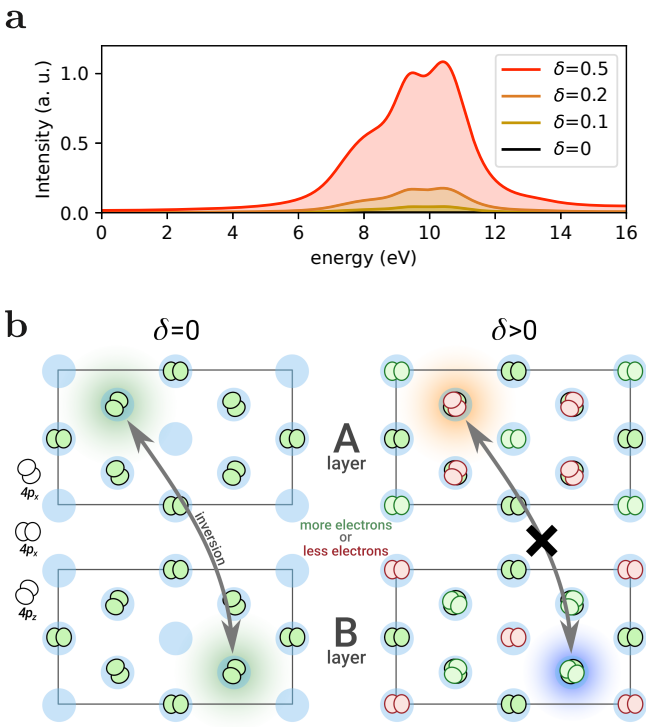

FIG. 3. **Energy dependence of the scattering amplitude in the orbital ordered phase.** (a) Expected energy dependence of the scattering amplitude, with its characteristic resonance structure, based on the square of the orbital-resolved projected densities of states (see Supplemental Material), and broadened to reflect the effect of finite lifetimes. Different curves represent different values of the relative phase shift between CDW components. The energy scale on the horizontal axis is measured with respect to the Fermi level. (b) Ti $4p$ orbital densities at fixed energy in the atomic structures with zero (left) and non-zero (right) relative phase shift δ between CDW components. For $\delta = 0$, three out of four Ti sites have one predominant $4p$ orbital (green), while orbitals with lower density are degenerate. The structures in neighboring planes are related by inversion. For nonzero relative phase shift, the densities of some previously degenerate orbitals increase (green) or decrease (red). The pattern of orbital polarization shown here for Ti $4p$ orbitals is also present in the densities of other orbitals, and breaks both inversion and three-fold rotational symmetry.

microscopic insight into the effects of orbital order, we consider structures with different phase shifts and calculate projected density of states (PDOS) by means of density functional theory (DFT) calculations. As resonant peaks are underlain by uneven orbital occupations [51–54], the RXS structure factor is proportional to a linear combination of the PDOS for all Ti atoms in the unit cell. In Fig. 3a, we demonstrate that a particular linear combination of Ti-$4p$ orbitals reflecting the expected difference in orbital occupation between consecutive layers, yields a nonzero scattering amplitude in structures with nonzero relative phase shifts.

As shown schematically in Fig. 3b, the onset of this signal implies differences between the densities of symmetry-related orbitals at fixed energy, and indicates a breakdown of both inversion and three-fold rotational symmetries. The presence of orbital order thus allows for resonant reflections that are forbidden in the CDW structure without relative phase shifts. Notice that because $TiSe_2$ is a weakly coupled material, the absolute variations in orbital occupation may be expected to be much lower than those in strongly correlated insulators, such as the archetypical orbitally-ordered material $LaMnO_3$ [40]. Nevertheless, a systematic investigation of which forbidden peaks become allowed and gain significant amplitude in the OO phase (see Supplemental Material), shows that both the momenta at which such reflections emerge, and the energy dependence of the predicted signal, are consistent with the RXS experiments.

CONCLUSIONS

We report experimental evidence for the existence of orbital order in the low-temperature phase of $1T$-$TiSe_2$, consistent with first-principles predictions based on a theoretical model for combined charge and orbital order.

These observations pave the way for exploring orbital order in other low-dimensional, weakly coupled materials. Based on the general nature of the mechanism stabilising the OO phase, one expects very similar types of orbital order to be common in determining physical properties throughout TMDC with commensurate multi-component charge order, like $2H$-TaS_2 or $1T$-VSe_2, but also more generally in beyond-graphene Van der Waals materials.

As all charge transfer processes take place within individual $TiSe_2$ sandwiches, the orbital order is expected to survive even in the monolayer limit. This, together with the strong interplay between orbital occupation and charge, lattice, and spin degrees of freedom, gives great potential to the orbital order as a promising route to tuning and manipulating the physical responses in devices based on Van der Waals materials.

ACKNOWLEDGEMENTS

Y.Y.P. is grateful for financial support from the National Natural Science Foundation of China (Grant No. 11974029). P.A. acknowledges support from the Gordon and Betty Moore Foundation, grant no. GMBF-9452. RXS experiments were supported by the U.S. Department of Energy grant no. DE-FG02-06ER46285, with use of the Advanced Photon Source supported by DOE contract no. DE-AC02-06CH11357. H.X.L. acknowledges financial support from the National Natural Science Foundation of China (No. 11922415). J.v.d.B acknowledges the Deutsche Forschungsgemeinschaft (DFG) for support

through the Würzburg-DresdenCluster of Excellence on Complexity and Topology in Quantum Matter – ct.qmat (EXC 2147, project-id 39085490) and the Collaborative Research Center SFB 1143 (project-id 247310070).

AUTHOR CONTRIBUTIONS

J.v.d.B., P.A., Y.Y.P. and J.v.W. conceived and designed the experiments and calculations; Y.Y.P. and X.F.G. performed the RXS experiment at Advanced Photon Source with the help of J.S. and Y.C.. H.X.L and D.Y. grew the $TiSe_2$ samples; S.J and Y.Q.H performed the resistivity measurement; Y.Y.P., Q.X, Q.Z.L and X.F.G analysed the experimental data; J.v.W. modelled atomic displacements and O.J. performed the first-principles calculations; J.v.W. wrote the manuscript with input from all authors.

METHODS

Sample preparation

We synthesised 1T-$TiSe_2$ single crystals in two steps. Firstly, polycrystalline 1T-$TiSe_2$ powders were synthesized in solid state, by grinding stoichiometric quantities of the reactants of Ti (Alfa Aesar, 99.9%) and Se (Alfa Aesar, 99.999%) in an agate mortar. The mixture was then transferred to a quartz tube and sealed under high vacuum. Polycrystalline samples were obtained after heating at 550°C for 120 hours. Secondly, single crystals of 1T-$TiSe_2$ were grown using the chemical vapor transport (CVT) method, with I_2 as the transport agent. The as-prepared polycrystalline 1T-$TiSe_2$ powders were mixed with I_2 in a quality ratio of about 20:1. The mixtures sealed in vacuum quartz tubes were then heated for 7 days in a two-zone furnace, where the source and growth zone temperatures were 700°C and 600°C, respectively. Resistivity measurements using the four-points method were performed on single crystals taken from the same batch of samples as that used for RXS experiments.

RXS measurements

The RXS experiments were performed at beam line 4-ID-D of the Advanced Photon Source at Argonne National Laboratory. The $TiSe_2$ crystal was mounted on an aluminum sample holder and cooled with a closed-cycle cryostat attached to a four-circle diffractometer. Experiments were done by integrating over all scattered photon energies. The linear polarization was collected with σ-incident polarization (perpendicular to the scattering plane). The X-ray absorption spectrum (XAS) was obtained by integrating the fluorescence signal. The observed pre-edge feature in these spectra is well-known to be related to the d-electrons [50]. The temperature dependence of T_{CDW} can be well-fitted using the empirical function $f(t) = I_0[1 - [(t+\alpha)/(1+\alpha))]^{\beta}]$, with $t = T/T_{\mathrm{CDW}}$ the reduced temperature, and α, β, and T_{CDW} used as fitting parameters [55].

First principles prediction of RXS intensities.

We perform density-functional-theory band-structure calculations using the generalized gradient approximation [56], as implemented in the full-potential code FPLO version 18 [57]. Although the structures without relative phase shifts feature a higher symmetry than those with phase shifts, we perform all calculations within the same low-symmetry monoclinic space group $C2$ to ensure that all structures are treated on equal footing. The low symmetry of the unit cell gives rise to numerical noise in the calculated projected DOS, which we remedy by using a densely sampled k-mesh of $41 \times 41 \times 24$ points (20213 points in the irreducible wedge).

* yingying.peng@pku.edu.cn
† vanwezel@uva.nl

[1] Otrokov, M. M. *et al.* Prediction and observation of an antiferromagnetic topological insulator. *Nature (London)* **576**, 416–422 (2019).
[2] Li, T. *et al.* Pressure-controlled interlayer magnetism in atomically thin CrI_3. *Nat. Mater.* **18**, 1303–1308 (2021).
[3] Chen, W. *et al.* Direct observation of van der Waals stacking–dependent interlayer magnetism. *Science* **366**, 983–987 (2019).
[4] MacNeill, D. *et al.* Gigahertz Frequency Antiferromagnetic Resonance and Strong Magnon-Magnon Coupling in the Layered Crystal $CrCl_3$. *Phys. Rev. Lett.* **123**, 047204 (2019).
[5] Gong, C., Kim, E. M., Wang, Y., Lee, G. & Zhang, X. Multiferroicity in atomic van der Waals heterostructures. *Nat. Commun.* **10**, 2657 (2019).
[6] Kang, S. *et al.* Coherent many-body exciton in van der Waals antiferromagnet $NiPS_3$. *Nature (London)* **585**, 785–789 (2021).
[7] Wu, Y. *et al.* Néel-type skyrmion in WTe_2/Fe_3GeTe_2 van der Waals heterostructure. *Nat. Commun.* **11**, 3860 (2020).
[8] Devarakonda, A. *et al.* Clean 2D superconductivity in a bulk van der Waals superlattice. *Science* **371**, 231–236 (2020).
[9] Noguchi, R. *et al.* Evidence for a higher-order topological insulator in a three-dimensional material built from van der Waals stacking of bismuth-halide chains. *Nat. Mater.* **20**, 473–479 (2021).
[10] Diego, J. *et al.* van der Waals driven anharmonic melting of the 3D charge density wave in VSe_2. *Nat. Commun.* **12**, 598 (2021).
[11] Geim, A. K. & Grigorieva, I. V. *Nature* **499**, 419 (2013).
[12] Novoselov, K. S., Mishchenko, A., Carvalho, A. & Castro Neto, A. H. *Science* **353**, aac9439 (2016).
[13] Kusmartseva, A. F., Sipos, B., Berger, H., Forró, L. & Tutiš, E. Pressure induced superconductivity in pristine $1t-tise_2$. *Phys. Rev. Lett.* **103**, 236401 (2009).

[14] Morosan, E. *et al. Nature Physics* **2**, 544–550 (2006).

[15] Li, L. J. *et al. Nature* **529**, 185–189 (2016).

[16] Di Salvo, F. J., Moncton, D. E. & Waszczak, J. V. Electronic properties and superlattice formation in the semimetal tise$_2$. *Phys. Rev. B* **14**, 4321–4328 (1976).

[17] Rossnagel, K., Kipp, L. & Skibowski, M. Charge-density-wave phase transition in 1t-tise$_2$: Excitonic insulator versus band-type jahn-teller mechanism. *Phys. Rev. B* **65**, 235101 (2002).

[18] Wilson, J. A. Concerning the semimetallic characters of tis$_2$ and tise$_2$. *Solid State Comm.* **22**, 551–553 (1977).

[19] Cercellier, H. *et al.* Evidence for an excitonic insulator phase in 1t-tise$_2$. *Phys. Rev. Lett.* **99**, 146403 (2007).

[20] Hughes, H. P. Structural distortion in tise$_2$ and related materials - a possible jahn-teller effect? *J. Phys. C: Solid State Phys.* **10**, L319–L323 (1977).

[21] Suzuki, N., Yamamoto, A. & Motizuki, K. Microscopic theory of the cdw state of 1t-tise$_2$. *J. Phys. Soc. Jpn.* **54**, 4668 (1985).

[22] Kidd, T. E., Miller, T., Chou, M. Y. & Chiang, T.-C. Electron-hole coupling and the charge density wave transition in tise$_2$. *Phys. Rev. Lett.* **88**, 226402 (2002).

[23] Calandra, M. & Mauri, F. *Phys. Rev. Lett.* **106**, 196406 (2011).

[24] Kogar, A. *et al.* Signatures of exciton condensation in a transition metal dichalcogenide. *Science* **358**, 1314–1317 (2017).

[25] van Wezel, J., Nahai-Williamson, P. & Saxena, S. S. *Phys. Rev. B* **81**, 165109 (2010).

[26] van Wezel, J. Chirality and orbital order in charge density waves. *EPL* **96**, 67011 (2011).

[27] Castellan, J.-P. *et al.* Chiral Phase Transition in Charge Ordered 1T-TiSe$_2$. *Phys. Rev. Lett.* **110** (2013).

[28] Gradhand, M. & van Wezel, J. Optical gyrotropy and the nonlocal Hall effect in chiral charge-ordered TiSe$_2$. *Phys. Rev. B* **92**, 041111 (2015).

[29] Hildebrand, B. *et al.* Local real-space view of the achiral 1 t- tise 2 2× 2× 2 charge density wave. *Physical review letters* **120**, 136404 (2018).

[30] Lin, M.-K., Hlevyack, J. A., Chen, P., Liu, R.-Y. & Chiang, T.-C. Comment on "Chiral Phase Transition in Charge Ordered 1T-TiSe$_2$". *Phys. Rev. Lett.* **122**, 229701 (2019).

[31] Rosenkranz, S., Osborn, R. & van Wezel, J. Rosenkranz, Osborn, and Van Wezel Reply:. *Phys. Rev. Lett.* **122**, 229702 (2019).

[32] Tokura, Y. & Nagaosa, N. Orbital physics in transition-metal oxides. *science* **288**, 462–468 (2000).

[33] Ritschel, T. *et al. Nature Physics* **11**, 328–331 (2015).

[34] Silva, A. & van Wezel, J. *SciPost Phys.* **4**, 028 (2018).

[35] Flicker, F. & van Wezel, J. *Phys. Rev. B* **94**, 235135 (2016).

[36] Kugel, K. I. & Khomskii, D. I. Crystal-structure and magnetic properties of substances with orbital degeneracy. *Zh. Eksp. Teor. Fiz* **64**, 1429–1439 (1973).

[37] Kugel, K. I. & Khomskii, D. I. The jahn-teller effect and magnetism: transition metal compounds. *Soviet Physics Uspekhi* **25**, 231 (1982).

[38] Moussa, F. & Villain, J. Spin-wave lineshape in two-dimensional k2cuf4: neutron experiments and theory. *J. Phys. C* **9**, 4433 (1976).

[39] Takata, M., Nishibori, E., Kato, K., Sakata, M. & Moritomo, Y. Direct observation of orbital order in manganites by mem charge-density study. *J. Phys. Soc. Japan* **68**, 2190–2193 (1999).

[40] Murakami, Y. *et al.* Resonant x-ray scattering from orbital ordering in lamno 3. *Physical review letters* **81**, 582 (1998).

[41] Staub, U. *et al.* Charge/orbital ordering vs. jahn-teller distortion in la0. 5sr1. 5mno4. *EPL* **76**, 926 (2006).

[42] Whangbo, M. H. & Canadell, E. Analogies between the concepts of molecular chemistry and solid-state physics concerning structural instabilities. electronic origin of the structural modulations in layered transition metal dichalcogenides. *J. Am. Chem. Soc.* **114**, 9587–9600 (1992).

[43] Iavarone, M. *et al.* Evolution of the charge density wave state in cu x tise 2. *Physical Review B* **85**, 155103 (2012).

[44] Xu, S.-Y. *et al.* Spontaneous gyrotropic electronic order in a transition-metal dichalcogenide. *Nature* **578**, 545–549 (2020).

[45] van Wezel, J. Polar charge and orbital order in 2h-tas$_2$. *Phys. Rev. B* **85**, 035131 (2012).

[46] Silva, A., Henke, J. & van Wezel, J. Elemental chalcogens as a minimal model for combined charge and orbital order. *Phys. Rev. B* **97**, 045151 (2018).

[47] Vedrinskii, R., Kraizman, V., Novakovich, A., Demekhin, P. V. & Urazhdin, S. Pre-edge fine structure of the 3d atom k x-ray absorption spectra and quantitative atomic structure determinations for ferroelectric perovskite structure crystals. *Journal of Physics: condensed matter* **10**, 9561 (1998).

[48] De Groot, F., Vankó, G. & Glatzel, P. The 1s x-ray absorption pre-edge structures in transition metal oxides. *Journal of Physics: Condensed Matter* **21**, 104207 (2009).

[49] Ueda, H. *et al.* Correlation between electronic and structural orders in 1$t-$Tise$_2$. *Phys. Rev. Research* **3**, L022003 (2021).

[50] Yamamoto, T. Assignment of pre-edge peaks in k-edge x-ray absorption spectra of 3d transition metal compounds: electric dipole or quadrupole? *X-Ray Spectrometry* **37**, 572–584 (2008).

[51] Elfimov, I. S., Anisimov, V. I. & Sawatzky, G. A. Orbital ordering, jahn-teller distortion, and anomalous x-ray scattering in manganates. *Phys. Rev. Lett.* **82**, 4264–4267 (1999). URL `https://link.aps.org/doi/10.1103/PhysRevLett.82.4264`.

[52] Takahashi, M., Igarashi, J.-i. & Fulde, P. Anomalous x-ray scattering in lamno 3. *Journal of the Physical Society of Japan* **68**, 2530–2533 (1999). URL `https://doi.org/10.1143/JPSJ.68.2530`. https://doi.org/10.1143/JPSJ.68.2530.

[53] Mahadevan, P., Terakura, K. & Sarma, D. D. Spin, charge, and orbital ordering in la$_{0.5}$sr$_{1.5}$mno$_4$. *Phys. Rev. Lett.* **87**, 066404 (2001). URL `https://link.aps.org/doi/10.1103/PhysRevLett.87.066404`.

[54] Benedetti, P., van den Brink, J., Pavarini, E., Vigliante, A. & Wochner, P. Ab initio calculation of resonant X-ray scattering in manganites. *Phys. Rev. B* **63**, 060408 (2001).

[55] Joe, Y. I. *et al.* Emergence of charge density wave domain walls above the superconducting dome in 1T-TiSe$_2$. *Nat. Phys.* **10**, 421 (2014).

[56] Perdew, J. P., Burke, K. & Ernzerhof, M. Generalized gradient approximation made simple. *Phys. Rev. Lett.* **77**, 3865–3868 (1996).

[57] Koepernik, K. & Eschrig, H. Full-potential nonorthogo-

nal local-orbital minimum-basis band-structure scheme.
Phys. Rev. B **59**, 1743–1757 (1999).

SUPPLEMENTAL MATERIAL

The supplementary information below includes details of RXS reflections and dichroism experiments not discussed in the main text, as well as the calculated structure factors for reflections that are forbidden in any configuration with simultaneous inversion and three-fold rotational symmetries.

X-ray scattering

Besides the $(0.5, 0, 0.5)$ reflection discussed in the main text, the orbital order in $TiSe_2$ can also be seen at other reflections forbidden in inversion and three-fold rotationally symmetric phases, such as the $(0.5, 0, 2.5)$ reflection shown in Fig. S1a. Similar to the $(0.5, 0, 0.5)$ reflection, Fig. S1b shows this peak to resonate at the pre-edge of the Ti K-edge, indicating its origin in variations of the occupation of Ti d-orbitals. Its onset temperature is $\sim$193 K (Fig. S1c), similar to that of the $(0.5, 0, 0.5)$ signal. This is confirmed by energy scans near the Ti K-edge as a function of temperature, shown in Fig. S2, indicating that the resonant behaviour for both reflections disappears above 193 K.

Besides the two classes of peaks discussed in the main text, one dominated by orbital order and the other by lattice displacements, we also observe a third group of reflections. An example of this is the peak at $(0.5, 0.5, 2.5)$, shown in Fig. S3. It resonates near the Ti K-edge rather than the pre-edge, and has an energy profile intermediate between the orbital and lattice dominated reflections. This is indicative of this peak originating from a combination of lattice and orbital scattering.

Finally, we explored the dependence of the four reflections $(0.5, 0.5, 0.5)$, $(0.5, 0, 0.5)$, $(0.5, 0.5, 2.5)$, and $(0.5, 0, 2.5)$ on the incident polarization, as shown in Fig. S4. We considered both linear and circular polarization, and our mea-

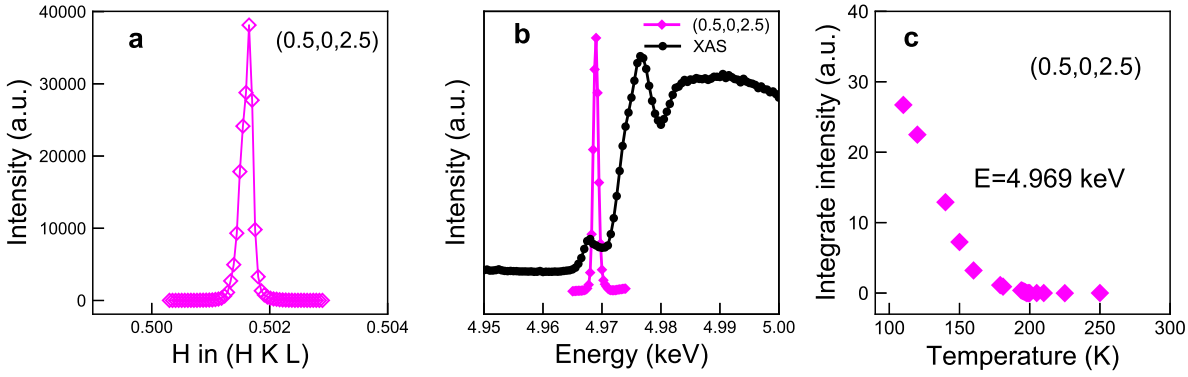

FIG. S1. **Orbital order in $TiSe_2$ measured by RXS at the Ti K-edge.** (a) H cut at 11 K for $(0.5, 0, 2.5)$. (b) Energy scans near the Ti K-edge at 11 K. The X-ray absorption spectrum is shown for comparison. (c) Temperature dependence of the integrated intensity for the $(0.5, 0, 2.5)$ peak taken at 4.969 keV.

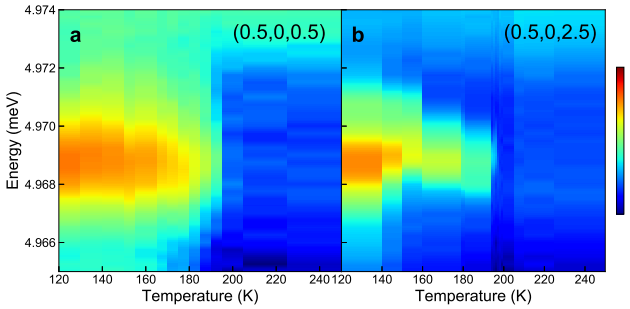

FIG. S2. **Temperature dependence of orbital-dominated reflections resonating at the pre-edge of the Ti K-edge.** (a, b) Temperature dependence for energy scans near the Ti K-edge for $(0.5, 0, 0.5)$ and $(0.5, 0, 2.5)$, respectively.

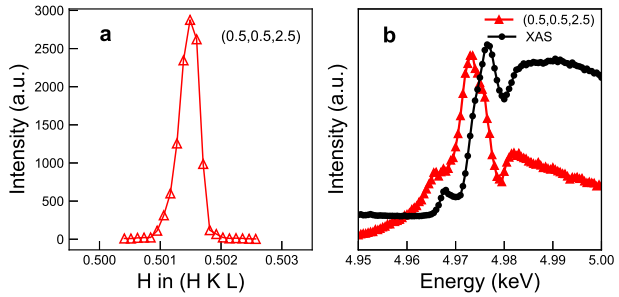

FIG. S3. **Charge and orbital order in $TiSe_2$ measured by RXS at the Ti K-edge.** (a) H cut at 11 K for (0.5,0.5,2.5). (b) Energy scans near the Ti K-edge. The X-ray absorption spectrum near the Ti K-edge is shown for comparison.

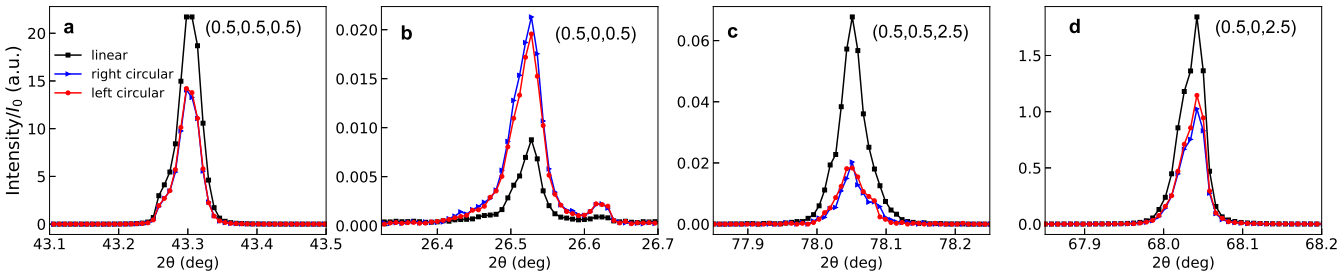

FIG. S4. **Polarization dependence of four reflections.** (a, b, c, d) θ-2θ scans taken at 4.969 keV with linear, right circular, and left circular polarizations for $(0.5, 0.5, 0.5)$, $(0.5, 0, 0.5)$, $(0.5, 0.5, 2.5)$ and $(0.5, 0, 2.5)$, respectively.

surement were done without an analyser resolving the polarization of the scattered signal. The data were normalized by the incident X-ray flux (I_0) for comparison. We did not find clear evidence for dichroism in these experiments. The side peaks or shoulders are due to small crystal mosaicity.

Atomic structure

The atomic positions used in the first-principles calculations discussed in the main text are listed in Table S1. Here, $\pm z_{\mathrm{Se}}$ is the fractional height of the Se atoms above and below the Ti plane. The CDW amplitude A is non-zero in the charge ordered phases, while γ is the ratio of Se to Ti electron-phonon coupling strengths. The parameter δ finally, represents a relative phase shift of the three CDW components, and is nonzero in the orbital-ordered phase.

The high-temperature pristine phase with $A = \delta = 0$ has space group $P\bar{3}m1$ (number 164). The symmetry is lowered to $P\bar{3}c1$ (number 165) when A is nonzero but δ remains zero. Notice that any distortions of this state that respect both inversion and three-fold rotational symmetry yield zero structure factors for reflections like $(0.5, 0, 0.5)$ and $(0.5, 0, 2.5)$. If δ becomes nonzero, both three-fold rotations and inversion symmetry are broken, and the space group reduces to $C2$ (number 5).

In Table S2, we list some of the peaks for which the combination of three-fold rotational and inversion symmetries dictates a zero structure factor in the high-temperature and charge ordered phases. For completeness, they are given in notation based on the trigonal unit cell for the high-temperature phase, as well as with respect to unit cells with the symmetries of the charge and orbital ordered phases. The sketch in Fig. S5 shows a comparison between the different unit cells and their momentum-space indices.

atom	x/a	y/b	z/c
Ti(1)	0	0	0
Ti(2)	$\frac{\sqrt{3}}{2}(1+2A)$	$\frac{1}{2}(-1-2A)$	0
Ti(3)	$\frac{\sqrt{3}}{2}(-1-2A)$	$\frac{1}{2}(-1-2A)$	0
Ti(4)	0	$1+2A$	0
Se(1)	$\frac{1}{\sqrt{3}}\left(1-\frac{3}{2}\delta\gamma A\right)$	$2\gamma A+\frac{1}{2}\delta\gamma A$	z_{Se}
Se(2)	$\frac{1}{2\sqrt{3}}\left(-1-6\gamma A+3\delta\gamma A\right)$	$\frac{1}{2}(1-2\gamma A-d\gamma A)$	z_{Se}
Se(3)	$\frac{1}{2\sqrt{3}}\left(-1+6\gamma A-3\delta\gamma A\right)$	$\frac{1}{2}\left(-1-2\gamma A-3\delta\gamma A\right)$	z_{Se}
Se(4)	$\frac{2}{\sqrt{3}}\left(-1+\frac{3}{4}\delta\gamma A\right)$	$\frac{3}{2}\delta\gamma A$	z_{Se}
Se(5)	$\frac{1}{\sqrt{3}}\left(-1+\frac{3}{2}\delta\gamma A\right)$	$2\gamma A-\frac{1}{2}\delta\gamma A$	$-z_{\mathrm{Se}}$
Se(6)	$\frac{1}{2\sqrt{3}}\left(1-6\gamma A-3\delta\gamma A\right)$	$\frac{1}{2}\left(-1-2\gamma A+d\gamma A\right)$	$-z_{\mathrm{Se}}$
Se(7)	$\frac{1}{2\sqrt{3}}\left(1+6\gamma A+3\delta\gamma A\right)$	$\frac{1}{2}\left(1-2\gamma A+3\delta\gamma A\right)$	$-z_{\mathrm{Se}}$
Se(8)	$\frac{2}{\sqrt{3}}\left(1-\frac{3}{4}\delta\gamma A\right)$	$-\frac{3}{2}\delta\gamma A$	$-z_{\mathrm{Se}}$

TABLE S1. Fractional atomic coordinates of a single $TiSe_2$ layer as a function of the structural parameters A, γ, δ, and z_{Se}. Adjacent layers of $TiSe_2$ have the same positions, but with A switching sign every layer.

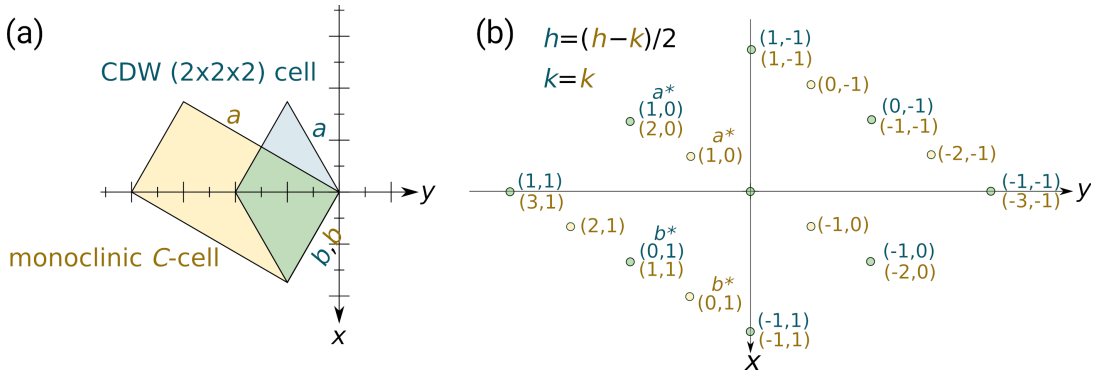

FIG. S5. **Comparison of unit cell geometries** (a) Real-space sketch of the unit cells associated with the charge (trigonal) and orbital ordered (monoclinic) phases. (b) Comparison of the corresponding momentum-space indices.

	trigonal unit cell $P\bar{3}m1$ (164)			enlarged trigonal unit cell $P\bar{3}c1$ (165)			monoclinic unit cell $C2$ (5)		
	$a = 3.535$ Å			$a = 7.07$ Å			$a = 12.2456$ Å		
							$b = 7.07$ Å		
	$c = 6.01$ Å			$c = 12.02$ Å			$c = 12.02$ Å		
							$\beta = 90°$		
d, Å	h	k	l	h	k	l	h	k	l
12.02000	0	0	$\pm 1/2$	0	0	± 1	0	0	± 1
5.45577	$1/2$	0	$\pm 1/2$	1	0	± 1	2	0	± 1
5.45577	0	$1/2$	$\pm 1/2$	0	1	± 1	1	1	± 1
5.45577	$1/2$	$-1/2$	$\pm 1/2$	1	-1	± 1	1	-1	± 1
5.45577	$-1/2$	$1/2$	$\pm 1/2$	-1	1	± 1	-1	1	± 1
5.45577	0	$-1/2$	$\pm 1/2$	0	-1	± 1	-1	-1	± 1
5.45577	$-1/2$	0	$\pm 1/2$	-1	0	± 1	-2	0	± 1
4.00667	0	0	$\pm 3/2$	0	0	± 3	0	0	± 3
3.35263	$1/2$	0	$\pm 3/2$	1	0	± 3	2	0	± 3
3.35263	0	$1/2$	$\pm 3/2$	0	1	± 3	1	1	± 3
3.35263	$1/2$	$-1/2$	$\pm 3/2$	1	-1	± 3	1	-1	± 3
3.35263	$-1/2$	$1/2$	$\pm 3/2$	-1	1	± 3	-1	1	± 3
3.35263	0	$-1/2$	$\pm 3/2$	0	-1	± 3	-1	-1	± 3
3.35263	$-1/2$	0	$\pm 3/2$	-1	0	± 3	-2	0	± 3
2.96669	1	0	$\pm 1/2$	2	0	± 1	4	0	± 1
2.96669	-1	0	$\pm 1/2$	-2	0	± 1	-4	0	± 1
2.96669	0	1	$\pm 1/2$	0	2	± 1	2	2	± 1
2.96669	1	-1	$\pm 1/2$	2	-2	± 1	2	-2	± 1
2.96669	-1	1	$\pm 1/2$	-2	2	± 1	-2	2	± 1
2.96669	0	-1	$\pm 1/2$	0	-2	± 1	-2	-2	± 1
2.43259	1	0	$\pm 3/2$	2	0	± 3	4	0	± 3
2.43259	0	1	$\pm 3/2$	0	2	± 3	2	2	± 3
2.43259	1	-1	$\pm 3/2$	2	-2	± 3	2	-2	± 3
2.43259	-1	1	$\pm 3/2$	-2	2	± 3	-2	2	± 3
2.43259	0	-1	$\pm 3/2$	0	-2	± 3	-2	-2	± 3
2.43259	-1	0	$\pm 3/2$	-2	0	± 3	-4	0	± 3

TABLE S2. Reflections whose structure factor is strictly zero in the high-temperature and charge ordered phases, but which become observable in the orbital ordered state. The three sets of indices are relevant to the unit cells of the high-temperature, charge-ordered, and orbital ordered phases.

Structure factors

With the atomic positions in Table S1, we can calculate the static structure factor, $S(\vec{k})$, which determines the scattering intensity in X-ray experiments. The contribution of a single atom at position $\vec{r}$ to the structure factor is:

$$S_{\vec{r}}(\vec{k}) = f(\vec{k})e^{i\,\vec{k}\cdot\vec{r}}. \tag{1}$$

Here, $f(\vec{k})$ is the atomic form factor for the atom at position $\vec{r}$, which varies for different species of atoms. For spherically symmetric atoms, the form factor depends only on the magnitude of the momentum. The total structure factor that determines the experimental response is the sum of atomic structure factors for all atoms in the unit cell. In resonant scattering experiments, the selective sensitivity to only a single intra-atomic transition implies that resonantly enhanced signals are dominated by only the contributions to the structure factor coming from a single species of atom. In the presence of orbital order, variations of orbital occupation moreover influence the number of electrons that can be resonantly excited between specific orbitals, effectively causing the atomic form factors for atoms with different orbital content to vary.

For a non-resonant scattering experiment, we can approximate all atomic form factors to be determined solely by the atomic species they refer to. Inserting the atomic positions (Table S1) of either all Ti atoms or all Se atoms into Eq. (1), the contribution of each atomic species to the structure factor can be determined. As long as the parameter δ is zero, we find that for any value of A, the total structure factor for peaks of the type $(h, 0, l)$ with h and l both half-integer is zero. The same holds for peaks of the type $(0, k, l)$ and $(h, -h, l)$ with h, k, and l all half-integer. In other words, reflections with these indices are forbidden in any structure with the space group $P\bar{3}c1$ associated with the charge ordered phase.

For atomic displacements that alter the space group, including those corresponding with non-zero δ, forbidden reflections may become allowed. The fact that this class of reflections is not observed in any non-resonant experiments is thus consistent with an atomic configuration in (or very close to) that of the charge ordered phase.

Turning to resonant scattering experiments next, we can model the effect of variations in orbital occupation by assigning different atomic form factors to atoms whose local density of states is predicted to be different in our first-principles calculation. This yields nonzero scattering intensities for all of the peaks listed in Table S2, which are forbidden reflections in the absence of orbital order.

Projected Density of States

For calculating the projected DOS of Ti $3d$ and $4p$ states, we use a local coordinate system with axes schematically illustrated in Fig. S6. Their directions in terms of orthogonal coordinates aligned with the crystallographic a and c axes in the high-temperature phase is given by $x = (-\sqrt{1/3}; 1; -\sqrt{2/3})$ and $z = (-\sqrt{1/3}; -1; -\sqrt{2/3})$. Note that we will also use $3d$ and $4p$ orbitals defined with respect to this local coordinate frame, rather than the crystallographic axes. Focusing on the azimuthal angle such that the a axis of the monoclinic unit cell lies in the plane formed by the incident and the scattered beam, the relevant projected Ti $4p$ and $3d$ orbital densities on atom j, $D_j(4p)$ and $D_j(3d)$, are given by:

$$\begin{aligned} D_j(3d) &= D_j(3d_{xz}) + e^{i\frac{2}{3}\pi}D_j(3d_{3z^2-r^2}) + e^{i\frac{4}{3}\pi}D_j(3d_{yz}) \\ D_j(4p) &= D_j(4p_y) + e^{i\frac{2}{3}\pi}D_j(4p_z) + e^{i\frac{4}{3}\pi}D_j(4p_x). \end{aligned} \tag{2}$$

The RXS structure factor for reflections that originate from orbital transitions rather than Thomson scattering in the low temperature phase and which are forbidden in the high temperature phase, is proportional to the difference between the orbital occupations on atoms whose locations are related by the inversion symmetry of the high temperature structure [51–54]. The following linear combination D of projected DOS D_j combines all such pairs:

$$D = D_{\mathrm{Ti(1)A}} + D_{\mathrm{Ti(4)A}} + e^{i\frac{2}{3}\pi}D_{\mathrm{Ti(2)A}} + e^{i\frac{4}{3}\pi}D_{\mathrm{Ti(3)A}} - D_{\mathrm{Ti(1)B}} - D_{\mathrm{Ti(4)B}} - e^{i\frac{2}{3}\pi}D_{\mathrm{Ti(2)B}} - e^{i\frac{4}{3}\pi}D_{\mathrm{Ti(3)B}}. \tag{3}$$

Here, A and B refer to the two layers within the unit cell, with for instance $D_{\mathrm{Ti(4)A}}$ denoting the projected DOS for atom Ti(4) in layer A. Using Eqns. 2 and 3, we can qualitatively estimate the RXS structure factor directly from the atom and orbital resolved DOS obtained in density-functional-theory band-structure calculations.

The resulting $D(3d)$ and $D(4p)$ are shown in Fig. S7. The small nonzero contributions for the case $\delta = 0$ have been verified to be numerical artifacts by confirming that their absolute values systematically decrease for denser k-meshes. Comparisons of the results for $\delta = 0.1$, $\delta = 0.2$ and $\delta = 0.5$ shows that the projected DOS increases systematically with δ. As the sign of the parameter δ is not fixed, we performed calculations also for the $\delta = -0.5$ case. The resulting plots are reflections in the $D = 0$ axis of the corresponding $\delta = 0.5$ curves.

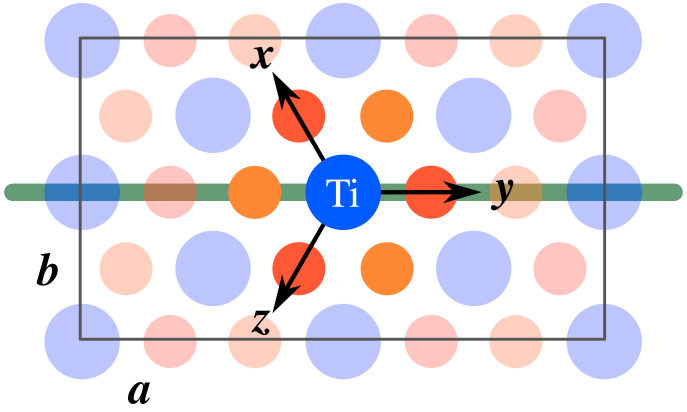

FIG. S6. **Choice of the local coordinate frame** The grey rectangle indicates the boundary of the monoclinic unit cell (space group C2, number 5). The green line indicates the plane containing the incident and scattered beams, which coincides with the projection of the local y axis onto the ab plane.

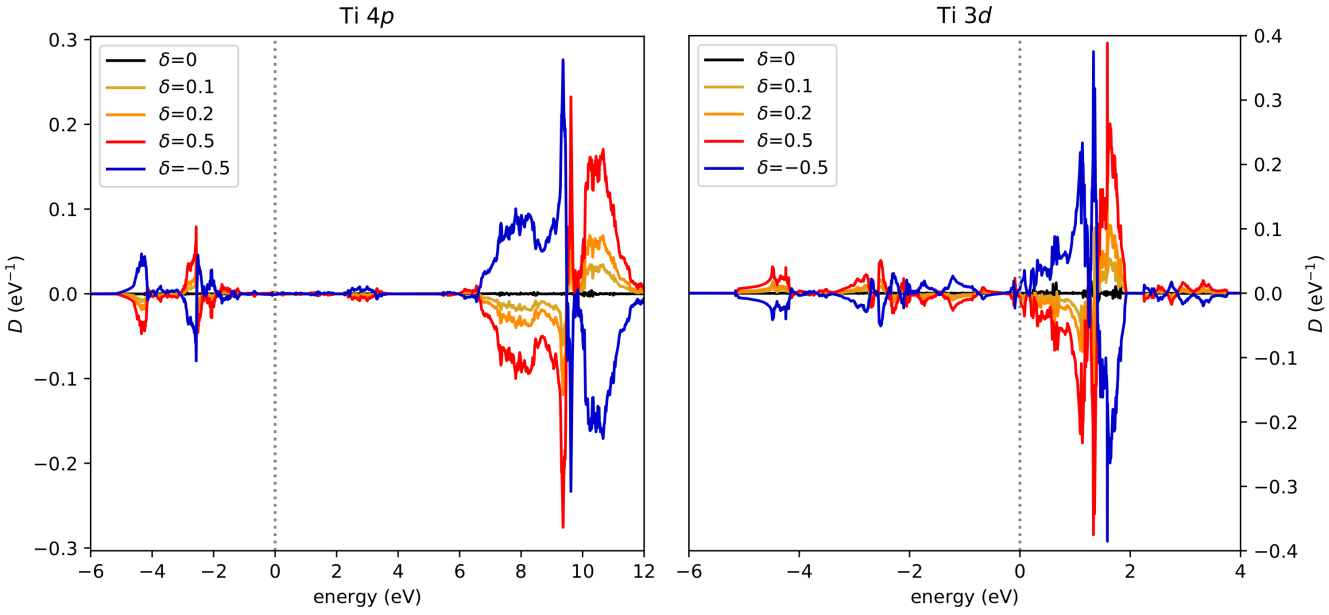

FIG. S7. **Projected Density of States** The linear combinations of Ti $4p$ (left) and $3d$ (right) projected DOS, as given by Eq. 3. The Fermi level is at zero energy. Small non-zero values of projected DOS for $\delta = 0$ are due to numerical noise.

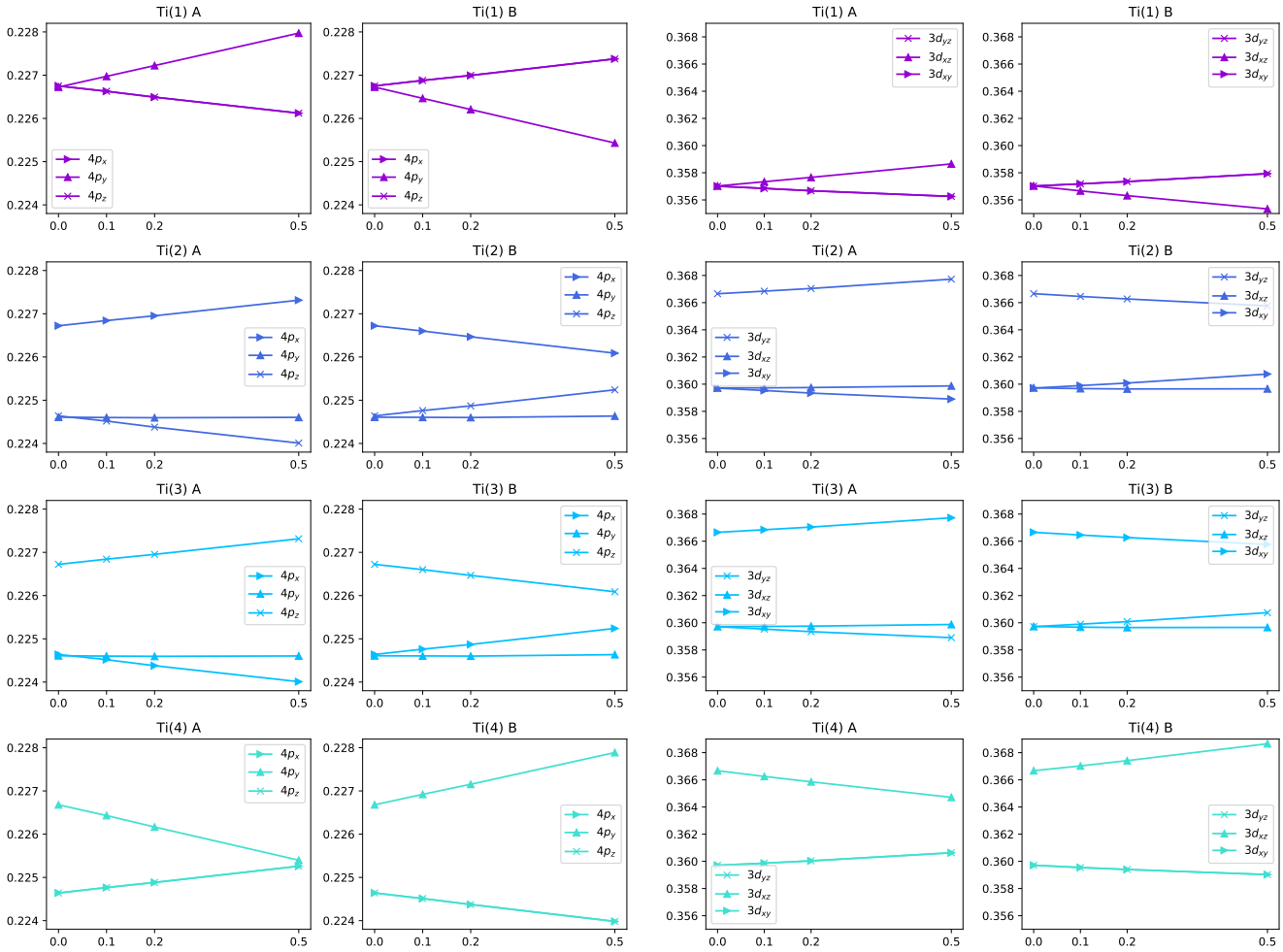

FIG. S8. **Orbital densities as a functions of the relative phase shift.** The densities of projected Ti $4p$ (left) and Ti $3d$ (right) orbitals are shown for the eight distinct Ti atoms in the monoclinic unit cell, as a function of δ. Coordinates for Ti atoms in layers A and B are given in Table S1 (note that the parameter A in that table changes sign depending on the layer), while orbitals are denoted with respect to the local coordinate axes.